

NUCLEOSYNTHESIS IN TYPE II SUPERNOVAE AND THE ABUNDANCES IN METAL-POOR STARS

TAKAYOSHI NAKAMURA, HIDEYUKI UMEDA¹, AND KEN'ICHI NOMOTO^{1,2}

Department of Astronomy, School of Science, University of Tokyo, Japan

AND

FRIEDRICH-KARL THIELEMANN²

Department für Physik und Astronomie, Universität Basel, Switzerland

AND

ADAM BURROWS²

Department of Astronomy, The University of Arizona, Tucson, AZ 85721, USA

ABSTRACT

We explore the effects on nucleosynthesis in Type II supernovae of various parameters (mass cut, neutron excess, explosion energy, progenitor mass) in order to explain the observed trends of the iron-peak element abundance ratios ($[Cr/Fe]$, $[Mn/Fe]$, $[Co/Fe]$ and $[Ni/Fe]$) in halo stars as a function of metallicity for the range $-4 \leq [Fe/H] \leq -2.5$. $[Cr/Fe]$ and $[Mn/Fe]$ decrease with decreasing $[Fe/H]$, while $[Co/Fe]$ behaves the opposite way and increases. We show that such behavior can be explained by a variation of mass cuts in Type II supernovae as a function of progenitor mass, which provides a changing mix of nucleosynthesis from an alpha-rich freeze-out of Si-burning and incomplete Si-burning. This explanation is consistent with the amount of ejected ^{56}Ni determined from modeling the early light curves of individual supernovae. We also propose that the metallicity of halo stars depends on the extent of the progenitors' Strömgren spheres in very early galaxies.

Subject headings: supernovae: general — Galaxy: halo — stars: abundances

1. INTRODUCTION

Very metal poor stars provide important clues to investigate early Galactic chemical and dynamical evolution because they contain valuable information about this time. We can learn how the Galaxy evolved chemically (as well as dynamically) in its early phase from the observation of these stars. Therefore, a large number of observations and abundance analyses have been performed. Until recently, no significant abundance change with metallicity had been observed. However, recent high-resolution abundance surveys have discovered interesting trends of $[Cr/Fe]$, $[Mn/Fe]$ and $[Co/Fe]$ with respect to $[Fe/H]$ ($[A/B] = \log_{10}(A/B) - \log_{10}(A/B)_{\odot}$). Both $[Cr/Fe]$ and $[Mn/Fe]$ decrease with decreasing metallicity from $[Fe/H] = -2.4$ to -4.0 , while $[Co/Fe]$ increases (Figure 1) (McWilliam et al. 1995a, 1995b; McWilliam 1997; see also Ryan et al. 1996 and reference therein).

Over the last few years, these trends have been the subject of controversy. McWilliam et al. (1995b) discussed the time-delay mechanism, which produces the abundance trends by the time-delay between SNe II with different masses or between SNe I and SNe II. They argued that this mechanism works for several species such as α -elements but has difficulties with the above trends. McWilliam et al. (1995b) also pointed out that the Galactic halo formation model proposed by Searle & Zinn (1978) is at odds with the time-delay mechanism. Instead, they suggested that the metallicity-dependent supernova progenitor mass function could explain these trends, while still being consistent with Searle & Zinn (1978). Audouze & Silk (1995) interpreted

the observations as evidence that the Galaxy was poorly mixed and proposed that at most two or three supernovae could have contaminated any particular cloud. In favor of this hypothesis, Ryan et al. (1996) proposed that a variation of the supernova explosion energy, which is connected with both the yields and the amount of ejecta dilution, could cause these trends. McWilliam (1997) and Searle & McWilliam (1998) suggested that diluting a primordial composition with solar composition supernova ejecta could explain the trends. In principle, hypothetical pre-galactic population III objects, such as very massive stars or pair creation supernovae (e.g., Bond et al. 1984), could be the cause of the observed behavior. However, none of these objects has been investigated in full detail in quantitative nucleosynthesis yield studies nor ever been incorporated in chemical evolution calculations.

Timmes et al. (1995) constructed a Galactic evolution model using a grid of Type II supernova models (Woosley & Weaver 1995, hereafter WW95), but did not explain the above-mentioned abundance trends. In Timmes et al. (1995), only the region with $[Fe/H] > -3.0$ was investigated, so that only limited information is available. However, their results seem to suggest that the metallicity effect alone cannot explain the observed trends.

The purpose of this paper is to provide a qualitative explanation of the halo abundance data within the framework of Type II supernovae (SNe II) explosive nucleosynthesis. It should be pointed out that self-consistent explosion and nucleosynthesis calculations, which start from core collapse, have not yet successfully determined the

¹the Research Center for the Early Universe, University of Tokyo, Japan

²Institute for Theoretical Physics, University of California, Santa Barbara, USA

mass cut between the central neutron star (or black hole) and the ejected envelope. Therefore, the mass cut of SNe II as a function of the progenitor mass is still an open question and can be treated as a free parameter. This investigation focuses on the mass cut, which determines the amount of ^{56}Ni in SN II ejecta, and its possible connection with the amount of (stable) Cr, Mn, Co, and Ni ejected. The connection between stellar evolution, explosive yields, and galactic evolution, observed via abundances in low metallicity stars, is made by performing chemical evolution studies in the framework previously described by Tsujimoto et al. (1995, 1997).

Although we are investigating the nucleosynthesis of low-metallicity stars, we use solar metallicity pre-supernova models in this paper for the following reasons. Previously, only WW95 calculated nucleosynthesis of SNe II using progenitor models with low metallicities; however, their progenitor models have not yet been published. Their results suggest that although the yields of iron peak elements depend on the progenitor metallicity, their variation in the range $Z = (10^{-2} - 10^{-4})Z_{\odot}$ is only about 20% or less. Since we are interested only in Z in this range, we neglect metallicity effects on progenitors and explore the dependence on other parameters, such as the stellar mass, mass cut, explosion energy, and neutron excess ($= 1 - 2Y_e$, where Y_e denotes the electron mole number). With this procedure, we can investigate the trends of the yields, i.e., how much the yields increase or decrease with these parameters.

In §2, we review the nucleosynthesis yields of SNe II (including their dependence on the mass cut, explosion energy, and Y_e of the innermost ejected matter). The results are applied in chemical evolution calculations in §3 in order to explore whether the observed abundance patterns in the metal-poor stars can be explained with our approach. Section 4 contains a more in-depth discussion, listing both the successes and the remaining open questions.

2. NUCLEOSYNTHESIS IN TYPE II SUPERNOVAE

2.1. Models

Stars initially more massive than $8M_{\odot}$ explode as SNe II at the end of their life, leaving neutron stars or black holes. When they explode, nucleosynthesis proceeds explosively because of high temperatures and densities in the deep stellar interior. In order to investigate the explosive nucleosynthesis of SNe II, we solve nuclear reaction networks, together with hydrodynamical equations, and calculate the energy generation by explosive burning.

Our calculations are performed in two steps. The first step is a hydrodynamical simulation of the SN II explosions with a small nuclear reaction network which contains only 13 alpha nuclei (^4He , ^{12}C , ^{16}O , ^{20}Ne , ^{24}Mg , ^{28}Si , ^{32}S , ^{36}Ar , ^{40}Ca , ^{44}Ti , ^{48}Cr , ^{52}Fe , and ^{56}Ni). The hydrodynamical simulations are carried out with a one dimensional PPM (piecewise parabolic method) code (Colella and Woodward 1984). We generate a shock by depositing thermal energy below the mass cut that divides the ejecta and the collapsing core, and perform the induced nucleosynthesis calculations following the procedure of our previous investigations (e.g. Hashimoto et al. 1989; Thielemann, Hashimoto, & Nomoto 1990; Thielemann, Nomoto, & Hashimoto 1996, hereafter TNH96). In the second step, at each mesh point

of the hydrodynamical model, post-processing calculations are performed with an extended reaction network (Hix & Thielemann 1996), which contains 211 isotopes, and provides precise total yields (also for minor abundances).

In our calculation, the progenitor models are taken from Nomoto & Hashimoto (1988, hereafter NH88). Figure 2 shows the Y_e profiles of the models ($25M_{\odot}$, $20M_{\odot}$ and $13M_{\odot}$) in NH88. In this paper, Y_e in the deep stellar interior is modified to take a constant value of Y_e^{deep} from $M_r = M_{\text{cut}}$ to $M_r = 1.70M_{\odot}$ (for the $25M_{\odot}$ star), $M_r = 1.64M_{\odot}$ ($20M_{\odot}$ star) and $M_r = 1.49M_{\odot}$ ($13M_{\odot}$ star). NH88's Y_e distribution of the progenitor is adopted for the outer region above the boundaries shown in Figure 2. Some of the adopted mass cuts are smaller than the Fe core masses obtained in the stellar evolution calculations (NH88). Note, however, that the Fe core mass, the Y_e profiles, and Y_e^{deep} are subject to uncertainties involved in the stellar evolution calculations, such as the treatment of convection, reactions rates (especially $^{12}\text{C}(\alpha, \gamma)^{16}\text{O}$), etc. Using the modified models, we analyze the dependences on the mass cut, Y_e , etc, and obtain some constraints on these parameters. We also treat mass cuts and explosion energies independently, though these are physically related, because of uncertainties in the explosion mechanism. When analyzing the yields, we do not include grid zones inside the mass cut in the ejecta by assuming that materials in these regions fall back onto a neutron star or a black hole. The change in the final total energy caused by this treatment is negligible.

In the following subsections, we show the dependence of SNe II yields on various parameters (mass cut, neutron excess, explosion energy, progenitor mass). Among them, the mass cut seems to be the most important parameter.

2.2. Production of iron-group elements in Type II supernovae

Figure 3 shows the isotopic composition of the ejecta of the explosion of the $20M_{\odot}$ star as a typical SN II. Here three distinctive regions are seen. One is the innermost high temperature region. The outer boundary of this region is determined by the condition that maximum temperatures of $T \gtrsim 5 \times 10^9 \text{ K}$ is attained behind the shock. In this region, nuclear statistical equilibrium (NSE) is achieved except for the slow triple-alpha process (α -rich freezeout). Thus, the nucleosynthesis depends only on Y_e and the entropy, being dominated by iron group elements (Woosley, Arnett, & Clayton 1973; Thielemann, Hashimoto, & Nomoto 1990). The most abundant element in this region of complete Si-burning with alpha-rich freeze-out is ^{56}Ni , provided $Y_e > 0.49$. The second region, which does not experience such high temperatures, undergoes incomplete Si-burning with only partial Si exhaustion; here the most abundant nucleus changes from ^{56}Ni to ^{28}Si . In the third region the temperatures are too low to produce any iron group elements, and only explosive O, Ne, or C-burning take place. Farther out in radius, regions are encountered where explosive nucleosynthesis barely affects the pre-explosive composition and matter as produced during the quasi-static evolution is ejected essentially unchanged.

In order to investigate the ratios [Cr/Fe], [Mn/Fe] and [Co/Fe] we look into the regions where these elements

are produced. First of all, ^{56}Ni , which decays into the most abundant Fe isotope ^{56}Fe , is produced not only in the complete Si-burning region but also in the incomplete Si-burning region. ^{52}Fe and ^{55}Co , which decay into ^{52}Cr and ^{55}Mn , respectively, are mostly synthesized in the incomplete Si-burning region. ^{52}Fe is also synthesized in the complete Si-burning region, but not a large amount. (Note that the ordinate of Figure 3 is log-scaled.) On the contrary, ^{59}Cu , which decays into ^{59}Co , is produced in the complete Si-burning region. Note that ^{55}Mn and ^{59}Co are the only stable isotopes of these elements and therefore, their abundances are identical with the Mn and Co element abundances. ^{52}Cr dominates the Cr element abundance by 84% (in solar composition). Thus, it is sufficient to take these isotopes into consideration when discussing the abundances of [Cr, Mn, Co/Fe].

2.3. Dependence on mass cuts

The above discussion suggests that the choice of the mass cut can affect the ratios [Cr/Fe], [Mn/Fe], and [Co/Fe]. For a deeper mass cut (i.e. smaller M_{cut}), the ejected mass of the complete Si-burning region is larger (i.e., the masses of Fe and Co are larger), while the ejected mass of the incomplete Si-burning region remains the same (i.e., the masses of Cr, Mn, and Fe are the same), accordingly the ratios of [Cr/Fe] and [Mn/Fe] are smaller and [Co/Fe] is larger. For a mass cut at larger radii (larger M_{cut}) these ratios show the opposite tendency. Therefore, specific choices of mass cuts in SNe II might explain the behavior of [Cr/Fe], [Mn/Fe], and [Co/Fe] in the metallicity range $-4 \leq [\text{Fe}/\text{H}] \leq -2.5$.

Table 1 summarizes the yields of the $25, 20 M_{\odot}$ stars for various mass cuts. Figure 4 shows the dependence of the abundance ratios on the mass cut. Here we use the solar abundances by Anders and Grevesse (1989). For smaller M_{cut} , [Cr/Fe] and [Mn/Fe] are smaller, while [Co/Fe] and [Ni/Fe] are larger. Note that stable Ni is dominated by ^{58}Ni and, thus, [Ni/Fe] is dominated by the $^{58}\text{Ni}/^{56}\text{Ni}$ ratio. One finds substantial ^{58}Ni production only in the inner complete Si-burning region, so that the behavior of [Ni/Fe] is similar to [Co/Fe]. The observational trends in Cr, Mn, Co and Ni are reproduced simultaneously.

2.4. Dependence on neutron excess

Figure 5 shows the Y_e dependence of SN II yields for $Y_e^{\text{deep}} = 0.4985$ (left) and 0.4950 (right). The progenitor is the $25M_{\odot}$ star with the $8M_{\odot}$ He core and the explosion energy is 1.0×10^{51} ergs. Table 2 summarizes the nucleosynthesis products and compares the abundance ratios with the solar ratios for different values of Y_e^{deep} . Figure 6 shows how these ratios depend on Y_e . For smaller Y_e (i.e., more neutron-rich environment), more ^{59}Cu (which decays into ^{59}Co) and ^{58}Ni are produced, while the yield of ^{52}Fe is smaller. ^{58}Ni is more sensitive to Y_e than ^{59}Co . The ^{56}Ni yield is smaller for smaller Y_e . Thus, all the metal to iron ratios are larger for smaller Y_e .

2.5. Dependence on explosion energy

The explosion energy of a typical SN II is considered to be $E \sim 1 \times 10^{51}$ ergs. For example, the explosion energy of SN 1987A has been estimated to be $E = (1.0 - 1.5) \times 10^{51}$

ergs from modeling of the early light curve (Shigeyama et al. 1987, 1988, 1990; Woosley et al. 1988; Nomoto et al. 1997; Nakamura et al. 1998). Figure 7 shows the energy dependence of Type II supernova yields for the same progenitor model, i.e., the $8M_{\odot}$ He core of the $25M_{\odot}$ star. Here $Y_e^{\text{deep}} = 0.4985$, while $E = 0.4 \times 10^{51}$ ergs (left) and 2.0×10^{51} ergs (right).

It is seen that the larger explosion energy forms a larger region of complete silicon burning, while the incomplete silicon burning region is enlarged only slightly. In other words, for larger E , the region of incomplete silicon burning is shifted outward in mass without an appreciable change of the enclosed mass. Therefore, the SN II with a larger explosion energy produces a larger amount of iron group elements if mass cuts are the same. That is, a larger explosion energy affects abundance ratios in the same way as a smaller mass cut. The explosion energy of SNe II can vary by a factor of five (Burrows 1998). We find that changing explosion energies from 0.4×10^{51} to 2.0×10^{51} ergs causes some changes in the abundance ratios, but cannot explain the large variations in the observations.

2.6. Dependence on progenitor mass

Figure 8 shows the progenitor mass dependence of SN II nucleosynthesis. The progenitors are the $6M_{\odot}$ He core of the $20M_{\odot}$ star (left) and the $8M_{\odot}$ He core of the $25M_{\odot}$ star (right). Both models have the same kinetic energy of the ejecta ($E = 1 \times 10^{51}$ ergs), but the deposited energies are different because of the difference in the gravitational potential energies between the two models. Y_e^{deep} is set to be 0.4985. Note that a more massive supernova has more massive complete and incomplete Si burning regions. As one can see in Figure 8, the mass ratio between the complete and incomplete Si-burning layers depends on the progenitor mass and the mass cut.

3. ABUNDANCE RATIOS IN METAL POOR STARS

More massive stars evolve faster. Thus, we expect the ejecta of the most massive stars to dominate the earliest phase of Galactic evolution, i.e. the period corresponding to the lowest [Fe/H]. If the mass cut M_{cut} between the ejecta and the neutron star tends to be smaller for the larger mass progenitor which provides earlier chemical input into the galactic evolution, one could expect to reproduce the observed trend in [Cr/Fe], [Mn/Fe] and [Co/Fe]. Whether this trend agrees quantitatively with the observations has to be tested.

The above trend between the progenitor mass and the mass cut cannot be monotonic because of two effects which compete with each other. One is the amount of neutrino absorbing matter, and the other is the depth of the gravitational potential. For intermediate massive stars, heavier stars eject relatively larger amounts of ^{56}Ni because of larger neutrino absorbing regions, while in more massive stars, such as SN1997D, the deeper gravitational potential wins and ^{56}Ni is scarcely ejected due to the fall back (Burrows 1998). Note that recent observations, relating the total ^{56}Ni mass to progenitor mass, seem to support this idea (see Figure 14).

We expect that the trend of increasing ^{56}Ni yield with increasing progenitor mass holds over a large range of

progenitor masses, while the reverse trend occurs more abruptly. Therefore, we focus here on the increasing trend (decreasing mass cut with increasing progenitor mass) up to a maximum progenitor mass, above which we assume that SNe II do not contribute to galactic chemical evolution.

Figure 9 shows the abundance ratios of various SN II models given in Table 3, where their parameters (mass cut, etc) are summarized. The abscissa of Figure 9 indicates only a model sequence (A-I). For these models, we take into account the observational trend between the ejected ^{56}Ni mass and stellar mass by assuming that the ^{56}Ni yield of the $25M_{\odot}$ star is larger than that of less massive stars (see Figure 14). Correspondingly, Figure 9 shows that deeper mass cuts yield smaller [Cr/Fe] and [Mn/Fe], while they lead to larger [Co/Fe]. This means that if supernovae at smaller [Fe/H] have deeper mass cuts, the observed trends can be explained.

We consider two models which may relate [Fe/H] and progenitor masses. One is the ‘mixed’ model, and the other is the ‘unmixed’ model. In the ‘mixed’ model, we assume that the mixing in the galactic scale is so efficient that the chemical uniformity is achieved in the early Galaxy. On the contrary, in the ‘unmixed’ model we assume that the mixing is not effective and the abundance ratios of a metal-poor star are the same as produced by a single SN II. We apply our results for each model. As described below, more massive supernovae correspond to smaller [Fe/H] in both models. After all, if more massive supernovae have deeper mass cuts, the trends in abundance ratios can be explained. It is noteworthy that recent observations of Ni mass in SNe II may support this idea (See §4.2).

Another important point is that [Co/Fe] and [Ni/Fe] are sensitive to Y_e^{deep} . As shown in §2.4 lower Y_e^{deep} results in higher [Co/Fe] and [Ni/Fe]. However, we can not reduce Y_e^{deep} too much, because stable Ni (^{58}Ni , ^{60}Ni , and ^{62}Ni) is overproduced and [Ni/Fe] becomes too high to be acceptable. With this constraint on Y_e^{deep} , [Co/Fe] is too small to be compatible with the observations. The deficiency of ^{59}Co (i.e., the deficiency of ^{59}Cu) is still an open question.

For these models, [Fe/H] is related to the stellar masses as follows. For the ‘mixed’ model, [Fe/H] at galactic time t_G , as well as other abundances (e.g. Cu, Mn, and Co), can be obtained by integrating the yields from all SNe exploded for $t < t_G$. [Fe/H] decreases monotonically towards the past and the age at the lower [Fe/H] corresponds to the shorter lifetime of more massive stars. In this way, we construct the Galactic halo model where the ages at [Fe/H] = -4 , -3 and -2.5 roughly coincide with the time when stars of $25M_{\odot}$, $20M_{\odot}$ and $13M_{\odot}$ exploded, respectively (Kobayashi 1998). Note that the mass vs. [Fe/H] relation is based on several assumptions (star formation rate, initial mass function, etc.), thus being subject to some uncertainties. The solid curves in Figure 10 show the changes in the iron-peak abundance ratios as a function of [Fe/H]. Three models are used to calculate these ratios, i.e., models ‘B’, ‘G’ and ‘H’ in Figure 9, and the Salpeter IMF of $\phi(M) \propto M^{-2.35}$ is adopted. The observed trends are well reproduced in Figure 10. But [Co/Fe] is too small. Since the absolute values of the yields are uncertain, we increase the amount of Co in order to compare the slope of

the curve with that of the observations. The dashed line in Figure 10 is such a model for which the amount of Co of the models ‘B’, ‘G’ and ‘H’ is increased by a factor of five. As we saw in §2.4, we can somewhat increase [Co/Fe] by reducing Y_e . The solid lines in Figure 11 show such a model, for which ‘D’, ‘G’ and ‘H’ are used. ‘D’ has the same mass cut as ‘B’, but has smaller Y_e . Although more Co is produced, this model has too high a [Ni/Fe] value because Y_e is too small.

In the ‘unmixed’ model, the next generation of stars were born in the ejecta of a SN II which is uncontaminated by previous SNe. Then these stars have the same heavy element abundance as a single SN II. In Figure 10, we show these ‘unmixed’ cases for the models ‘B’, ‘G’ and ‘H’ (filled circles). In this case, [Fe/H] depends on how much interstellar material is mixed with the ejecta before forming the next generation of stars. Thus it is not trivial to see why there is a relation between [Fe/H] and progenitor mass. In §4.1 we will propose a plausible model that the mixing takes place within the Strömgren radius around the progenitor. For now, we plot $M = 25$, 20 , and $13 M_{\odot}$ at [Fe/H] = -4 , -3 , and -2.5 , though the exact correspondence depends on the assumptions about the Strömgren radius. Filled triangles in Figure 10 indicate the models for which the amount of Co of the models ‘B’, ‘G’ and ‘H’ is multiplied by five. Filled squares in Figure 11 shows the same ‘unmixed’ model, but for models ‘D’, ‘G’ and ‘H’. As mentioned above, [Ni/Fe] values of these models are too high.

If we choose other set of models (e.g. ‘A’, ‘G’ and ‘I’), we enhance the contrast for both the mixed model and the unmixed model. In Figures 12 and 13, we show such models. The solid lines and filled circles in Figure 12 use ‘A’, ‘G’ and ‘I’, and the solid lines and filled squares in Figure 13 use ‘C’, ‘F’ and ‘T’. Filled triangles in Figure 12 indicate the models for which the amount of Co of the models ‘A’, ‘G’ and ‘I’ is multiplied by five. In these figures, we can see that the contrasts in [Cr/Fe] and [Mn/Fe] become larger, while contrasts in [Ni/Fe] and the amount of ^{56}Ni become too large, and the decline in [Co/Fe] is still too small. Hence, little advantage is seen.

The slope of the mixed model seems slightly too gentle, while the unmixed model can produce a steeper slope. We cannot say clearly which is better, the mixed model or the unmixed model. However, we prefer the unmixed model, which better reproduces the inclination of the [Co/Fe] vs. [Fe/H] curve.

4. DISCUSSION

4.1. Contamination by Type II supernovae in the very early Galaxy

As we saw in §3, we cannot say clearly which is better, the mixed model or the unmixed model. However, the mixed model tends to predict too small a metallicity dependence for the iron-peak element abundances. Indeed, Audouze & Silk (1995) and Ryan et al. (1996) argue that only one, or at most two to three, SNe could have contaminated a particular cloud in the [Fe/H] < -2.5 region. In the last section, we show that variations of [Cr/Fe], [Mn/Fe], and [Co/Fe] can be explained by the differences of progenitor masses. The question is then why there should be a tight correlation between [Fe/H] and the pro-

genitor mass.

The [Fe/H] of a star is determined by the amount of iron ejected from past supernovae and the mass of hydrogen in the mixing region. Our calculations show that in order to explain the large variations of the observed abundance ratios (e.g. -0.5 dex in [Cr/Fe]), each SN II must eject $0.05 \sim 0.2 M_{\odot}$ of iron, i.e., the amount of iron seems to fall into a relatively narrow range. So in the very low metallicity regions, the hydrogen mass determines [Fe/H]. In this case, there must be an order of magnitude difference in hydrogen mass for [Fe/H] in the range from -4 to -2.5 .

Ryan et al. (1996) presented an argument concerning the mass of the ISM (interstellar matter), m_{ISM} , mixed with the ejecta. They derive an analytic expression for m_{ISM} from eqs. (4.4b) and (3.33a) in Cioffi et al. (1988), and suggest that m_{ISM} depends only weakly on the environmental details, but strongly on the explosion energy of the supernova. According to Ryan et al., m_{ISM} changes almost linearly with explosion energy. However, the explosion energy can vary only by a factor of 5 (Burrows 1998), so it is difficult to make energy variation of m_{ISM} only by the difference in the explosion energy.

The above discussion is derived under the assumption that the ISM is uniform. However, there is a distinctive non-uniformity characterized by the “Strömgren sphere.” Within this sphere matter is ionized by photons, but outside this sphere matter is unionized. The progenitors of SNe II are very hot and luminous during their main sequence phase, so their Strömgren spheres are very large ($10 \sim 100$ pc). The essential point is that the Strömgren sphere likely determines the amount of hydrogen into which the ejecta of one supernova are mixed. The shock advances very easily within the Strömgren sphere, but is strongly decelerated outside the sphere, since it has to ionize the matter there. This means the effective adiabatic index γ approaches $\gamma \sim 1$. The radius of the Strömgren sphere is sensitive to the temperature of the star. The change of only 25% in the temperature of the star results in a doubling of the Strömgren radius (Osterbrock, 1989), which results in a factor of $2^3 = 8$ change in swept up hydrogen masses. Therefore, it is possible to explain the observed range in [Fe/H]. A more massive star has a larger Strömgren radius, so [Fe/H] in the shell becomes lower. Time estimates corroborate this possibility. The recombination time scale, i.e., the Strömgren sphere’s life time, is 10^5 to 10^6 years. Stellar evolution time after the main sequence phase, plus shock propagation time, is 10^5 to 10^6 years. So the Strömgren sphere produced during the main sequence phase survives until the SN II explosion and it coincides with the shock radius, while its radius depends on both progenitor mass and the number density of hydrogen in the ambient ISM per cubic centimeter, n_0 . We roughly estimate the hydrogen mass swept up by the shocks using low metal progenitor models (Schaller et al. 1992), that is, $4 \times 10^4 \cdot (n_0/1.0)^{-1} M_{\odot}$ for $25 M_{\odot}$ and $4 \times 10^3 \cdot (n_0/1.0)^{-1} M_{\odot}$ for $15 M_{\odot}$. From this estimate, the hydrogen masses differ as much as a factor of 10. However one should be cautious. For very small n_0 ($n_0 \sim 0.1$), the shock cannot reach the Strömgren radius, so the hydrogen mass cannot be determined by the Strömgren radius. On the other hand, for very large n_0 ($n_0 \sim 1$), the Strömgren sphere vanishes before being approached by the shock. In this case, however,

the contrast between more massive and less massive stars becomes more remarkable, for the longer life time of the latter makes it easier for the Strömgren sphere to vanish. This possibility is worth further investigation.

4.2. Mass of ^{56}Ni in Type II supernova ejecta

Our results in §3 suggest that a more massive supernova has a deeper mass cut, so that the ejected ^{56}Ni mass increases with the progenitor mass. The amount of ^{56}Ni should be determined by the competition between the amount of neutrino absorbing matter and the depth of the gravitational potential. Accordingly, the intermediate massive stars eject a relatively large amount of ^{56}Ni because of a large neutrino absorbing region, while in a more massive star the deeper gravitational potential wins and ^{56}Ni is scarcely ejected due to fallback.

This is consistent with recent ^{56}Ni mass estimates from light curve modeling for SNe II and Type Ib/Ic supernovae (SNe Ib/Ic) which are the explosions of bare cores of massive stars (Figure 14). From SN IIb 1993J (Nomoto et al. 1993; Iwamoto et al. 1997), SN Ic 1994I (Nomoto et al. 1994a; Iwamoto et al. 1994) and SN1987A (e.g. Nomoto et al. 1994b for a recent review), the $13 - 20 M_{\odot}$ stars eject $\sim 0.07 M_{\odot}$ ^{56}Ni . For $M > 20 M_{\odot}$, there has been little information, but recent SNe II/Ic suggest the strong mass-dependence of Fe yield. The light curve of SN Ic 1997ef indicate the production of $\sim 0.15 M_{\odot}$ of ^{56}Ni (Iwamoto et al. 1998a), while that of SN II 1997D shows the synthesis of only $\sim 0.002 M_{\odot}$ of ^{56}Ni from the $25 - 30 M_{\odot}$ star (Turatto et al. 1998). Such an observed mass dependence of the ^{56}Ni mass is consistent with the theoretical expectation.

For $M > 30 M_{\odot}$, we expect that little ^{56}Ni is ejected (WW95), because of a large amount of fall back, except for the hypernova case (Iwamoto et al. 1998b). On the other hand, the outer mantle including the oxygen-rich layer would be ejected from such a massive supernova. This is also required from the Galactic chemical evolution model (Tsujimoto et al. 1997).

4.3. The Galactic chemical evolution

In our new models, stars around $\sim 25 M_{\odot}$ have deeper mass cuts, thus ejecting a larger amount of Fe compared with the yields adopted by Tsujimoto et al. (1995). It would be interesting to examine the consequences of such a stellar-mass dependent Fe yield for the Galactic chemical evolution model and to compare with observations. For $[\text{Fe}/\text{H}] \lesssim -2.5$, however, the error bars of the abundances in metal-poor stars other than Cr, Mn, Co, Ni and Fe are still too large to make meaningful comparisons (Ryan 1998).

For $[\text{Fe}/\text{H}] \gtrsim -2.5$, we can assume that the ejecta from various SNe II are well mixed with ISM. Thus the abundance ratios between various elements and Fe are determined by the total amount of Fe ejected by previous SNe II. With the new choice of mass cuts, the total amount of Fe is almost the same as that in the previous model by Tsujimoto et al. (1995), because Tsujimoto et al. (1995) assumed that $13 - 15 M_{\odot}$ stars produce a larger amount of Fe than stars more massive than $20 M_{\odot}$, while in our new model $13 - 20 M_{\odot}$ stars produce smaller amounts of Fe than

more massive stars. These differences almost canceled out, leading to similar total Fe yield from SNe II.

Because the total Fe yield from SNe II is similar to Tsujimoto et al. (1995), the evolution of the abundance ratios such as [Cr/Fe] and [O/Fe] at $[\text{Fe}/\text{H}] \gtrsim -2.5$ in our model is similar to that in Tsujimoto et al. (1995), which is consistent with the observations. The evolution of the [Mn/Fe] ratio between $[\text{Fe}/\text{H}] = -2.5$ and -1.0 depends more on the SNe Ia rate rather than the SNe II rate (Kobayashi 1998). At $[\text{Fe}/\text{H}] < -1$, $[\text{Mn}/\text{Fe}] \sim -0.5$ due to SNe II. With increasing $[\text{Fe}/\text{H}]$, $[\text{Mn}/\text{Fe}]$ approaches the solar value because of the increasing contribution of SNe Ia, which have $[\text{Mn}/\text{Fe}] > 0$ according to SN Ia model W7 (Nomoto et al. 1984). Detailed Galactic halo chemical evolution models will be given in a separate paper.

The deficiency of ^{59}Co (i.e., ^{59}Cu) remains a problem. $[\text{Co}/\text{Fe}]$ did not reach zero at $[\text{Fe}/\text{H}] = 0$ in the above Galactic chemical evolution. The most important parameter which determines the abundance of ^{59}Cu is Y_e^{deep} (see §2.4). Lower Y_e^{deep} produces larger $[\text{Ni}/\text{Fe}]$ than $[\text{Co}/\text{Fe}]$, which results in a large deviation of $[\text{Ni}/\text{Fe}]$ from the observations. Therefore it seems unlikely that Y_e solves this problem. Could uncertainties in nuclear cross sections solve this problem? This may not be easy because NSE is almost achieved in the region where ^{59}Cu is produced. Thus, cross section differences will not have a large effect. There are other elements which decay into Co, but the amount of these elements is very small. The deficiency of Co has to be investigated further.

In this work, we used progenitor models with solar metallicity. Metallicity dependence does not affect our main conclusions, such that the mass cut can explain the interesting trends in abundance ratios, because the elements are produced in the same region, in the same way. However, some quantitative features, e.g., the absolute value of each yield, may be sensitive to metallicity. Two of us (H. U. & K. N.) are currently investigating such metallicity effects. There are other potentially important effects, such as instabilities, dynamic convection, and rotation. These effects also should be investigated in the future.

This work would not have been possible without the support of Institute for Theoretical Physics, University of California, Santa Barbara, USA, itself supported under NSF grant no. PHY74-07194. We would like to thank Raph Hix for providing us his nuclear reaction network code, Andrew McWilliam and Shigeru Kubono for helpful suggestions and comments, Sean Ryan for providing us with the data in his paper, Masaaki Hashimoto for providing us with progenitor models, and Chisato Ikuta for helping to gather observational data. The authors acknowledge helpful discussions with Toshikazu Shigeyama, Koichi Iwamoto and Chiaki Kobayashi on several points in this paper. Finally, we would like to thank the referee, F. X. Timmes, for useful comments to improve the paper. This work has been supported by the Swiss Nationalfonds grant (20-47252.96), by the US NSF under grant AST 96-17494, by the Grant-in-Aid for Scientific Research (05242102, 06233101), and by COE research (07CE2002) of the Japanese Ministry of Education, Science, and Culture.

REFERENCES

Anders, E., and Grevesse, M. 1989. *Geochim. Cosmochim. Acta*, 53, 197

Audouze, J., & Silk, J. 1995, *ApJ*, 451, L49

Bond, J. R., Arnett W. D., & Carr B.J. 1984, *ApJ*, 280, 825

Burrows, A. 1998, the 9'th Workshop on Nuclear Astrophysics, held at the Ringberg Castle, Germany, March 23 - 29, 1998, ed. E. Müller & W. Hillebrandt, p.76

Cioffi, D.F., McKee, C.F. & Bertschinger, E. 1988, *ApJ*, 334, 252

Colella, P., & Woodward, P. R. 1984, *J. Comput. Phys.* 54, 174

Gratton, R. G. 1989, *A&A*, 208, 171

Gratton, R. G. & Sneden, C. 1987, *A&A*, 178, 179

Gratton, R. G. & Sneden, C. 1988, *A&A*, 204, 193

Gratton, R. G. & Sneden, C. 1991, *A&A*, 241, 501

Hashimoto, M., Nomoto, K., & Shigeyama, T. 1989, *A&A*, 210, 5

Hix, W. R. & Thielemann, F.-K. 1996, *ApJ*, 460, 869

Iwamoto, K., Nomoto, K., Höflich, P., Yamaoka, H., Kumagai, S., & Shigeyama, T., 1994, *ApJ*, 437, L115

Iwamoto, K., Young, T. R., Nakasato, N., Shigeyama, T., Nomoto, K., Hachisu, I., & Saio, H., 1997, *ApJ*, 477, 865

Iwamoto, K., Nakamura, T., Nomoto, K., Mazzali, P. A., Garnavich, P., Kirshner, R., Jha, S., & Balam, D. 1998a, *ApJ*, submitted

Iwamoto, K., Mazzali, P. A., Nomoto, K., Umeda, H., Nakamura, T., Patat, F., Danziger, I. J., Young, T. R., Suzuki, T., Shigeyama, T., Augusteijn, T., Doublier, V., Gonzalez, J.-F., Boehnhardt, H., Brewer, J., Hainaut, O.R., Lidman, C., Leibundgut, B., Cappellaro, E., Turatto, M., Galama, T. J., Vreeswijk, P. M., Kouveliotou, C., Paradijs, J., van, Pian, E., Palazzi, E., & Frontera F., *Nature*, accepted, 1998b

Kobayashi, C. 1998, private communication

Magain, P. 1989, *A&A*, 209 211

McWilliam, A., Preston, G.W., Sneden, C., & Shectman, S. 1995a, *AJ*, 109, 2736

McWilliam, A., Preston, G.W., Sneden, C., & Searle, L. 1995b, *AJ*, 109, 2757

McWilliam, A. 1997, *ARA&A*, 35, 503

McWilliam, A. 1998, private communication

Molaro, P., & Bonifacio, P. 1990, *A&A*, 236, L5

Molaro, P., & Castelli, F. 1990, *A&A*, 228, 426

Nakamura, T., Iwamoto, K. & Nomoto, K. 1998, in *Origin of Matter and Evolution of Galaxies in the Universe*, eds. T. Kajino, & S. Kubono, (World Scientific Publishing)

Nomoto, K. Thielemann, F.-K., & Yokoi, K. 1984, *ApJ*, 286, 644

Nomoto, K. & Hashimoto, M. 1988, *Phys. Rep.*, 256, 173

Nomoto, K., Suzuki, T., Shigeyama, T., Kumagai, S., Yamaoka, H., and Saio, H. 1993, *Nature*, 364, 507

Nomoto, K., Yamaoka, H., Pols, O. R., Van Den Heuvel, E. P. J., Iwamoto, K., Kumagai, S., & Shigeyama, T. 1994a, *Nature*, 437, 115

Nomoto, K., Yamaoka, H., Shigeyama, T., Kumagai, S., & Tsujimoto, T. 1994b, in *Supernovae, Les Houches Session LIV*, ed. S. A. Bludman et al. (Amsterdam: North-Holland), 199

Nomoto, K., Blinnikov, S.I., & Iwamoto, K. 1997, "Modeling the Light Curve of SN 1987A", The Fifth CTIO/ESO/LCO Workshop, SN1987A: Ten Years After, eds. M. Phillips, & N. Suntzeff (PASP Conference series)

Norris, J. E., Peterson, R. C., & Beers, T. C. 1993, *ApJ*, 415, 797

Osterbrock, D. E. 1989, "Astrophysics of Gaseous Nebulae and Active Galactic Nuclei", University Science Books

Peterson, R. C., Kurucz, R. L., & Carney, B. W. 1990, *ApJ*, 350, 173

Primas, F., Molaro, P., & Castelli, F. 1994, *A&A*, 290, 885

Ryan, S.G., & Norris, J.E. 1991, *AJ*, 101, 1835

Ryan, S.G., Norris, J.E., & Beers, T.C. 1996, *ApJ*, 471, 254

Ryan, S.G. 1998, private communication

Searle, L. & Zinn, T. 1978, *ApJ*, 225, 357

Searle, L. & McWilliam, A. 1998, in preparation

Shigeyama, T., Nomoto, K., Hashimoto, M., & Sugimoto, D. 1987, *Nature*, 328, 320

Shigeyama, T., Nomoto, K., & Hashimoto, M. 1988, *A&A*, 196, 141

Shigeyama, T., & Nomoto, K., 1990, *ApJ*, 360, 242.

Shigeyama, T., Suzuki, T., Kumagai, S., Nomoto, K., Saio, H., & Yamaoka, H., 1994, *ApJ*, 420, 341.

Thielemann, F.-K., Hashimoto, M., & Nomoto, K. 1990, *ApJ*, 349, 222

Thielemann, F.-K., Nomoto, K., & Hashimoto, M. 1996, *ApJ*, 460, 408

Timmes, F. X., Woosley, S. E., Weaver, T. A. 1995, *ApJS*, 98, 617

Tsujimoto, T., Nomoto, K., Yoshii, Y., Hashimoto, M., Yanagida, Y., & Thielemann, F.-K. 1995, *MNRAS*, 277, 945

Tsujimoto, T., Yoshii, Y., Nomoto, K., Matteucci, F., Thielemann, F.-K. & Hashimoto, M. 1997, *ApJ*, 483, 228

Turatto, M., Mazzali, P. A., Young, T. R., Nomoto, K., Iwamoto, K., Benetti, S., Cappellaro, E., Danziger, I. J., de Mello, D. F., Phillips, M. M., Suntzeff, N. B., Clocchiatti, A., Piemonte, A., Leibundgut, B., Covarrubias, R., Maza, J., Sollerman, J., 1998, *ApJ*, in press

Woosley, S.E., Arnett, W. D., Clayton, D. D. 1973, *ApJS*, 26, 231

Woosley, S.E., Pinto, P.A., & Enzman, L. 1988, *ApJ*, 324, 466

Woosley, S.E., & Weaver, T.A. 1995, *ApJS*, 101, 181

Zhao, G. & Magain, P. 1990, *A&A*, 238, 242

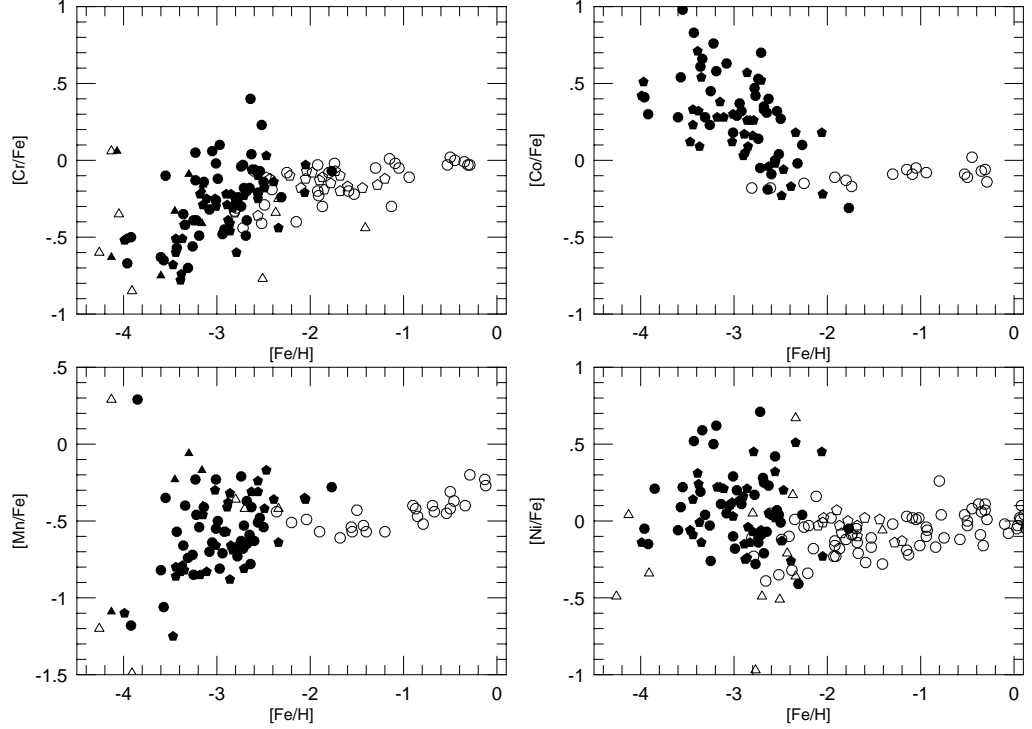


FIG. 1.— The trends of iron-peak abundance ratios. These data are from Ryan et al. (1991, 1996) (filled circles); McWilliam et al. (1995a), McWilliam (1998) (filled pentagons); Norris et al. (1993), Primas et al. (1994) (filled triangles); Gratton & Sneden (1987, 1988, 1991), and Gratton (1989) (open circles); Magain (1989), and Zhao & Magain (1990) (open pentagons); and Molaro & Bonifacio (1990), Molaro & Castelli (1990), Peterson et al. (1990) (open triangles).

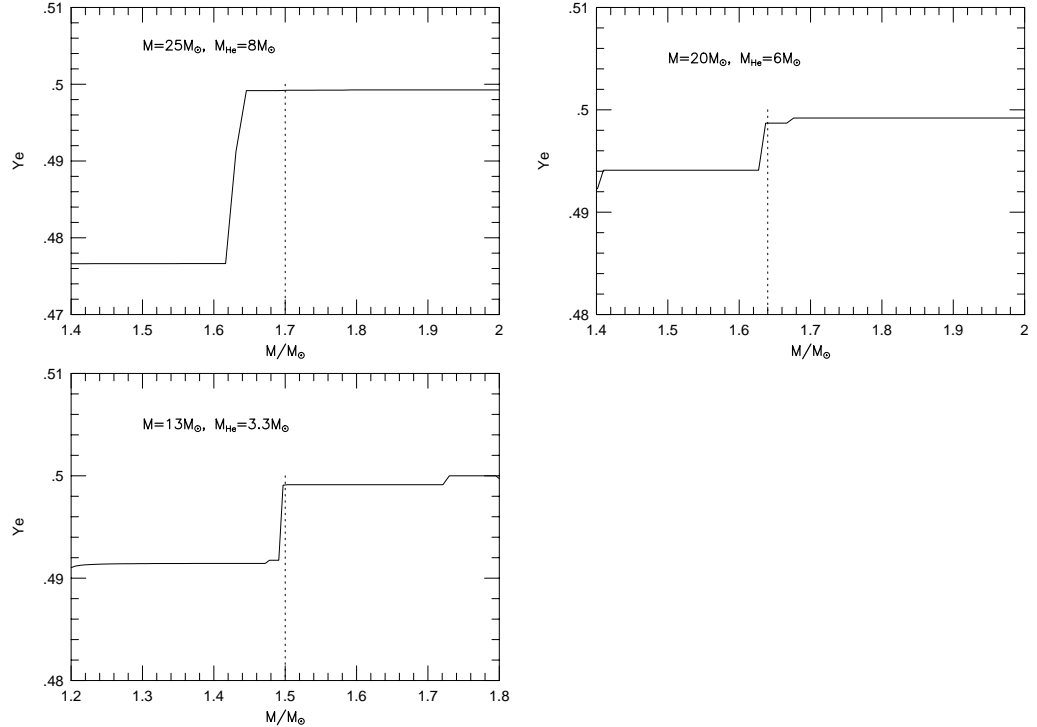


FIG. 2.— Y_e profiles of the models in NH88. Dotted lines indicate the boundaries of Y_e modification. In our calculations, Y_e is modified to be a constant value below these lines, while the NH88's Y_e distribution of the progenitor models is maintained above these lines.

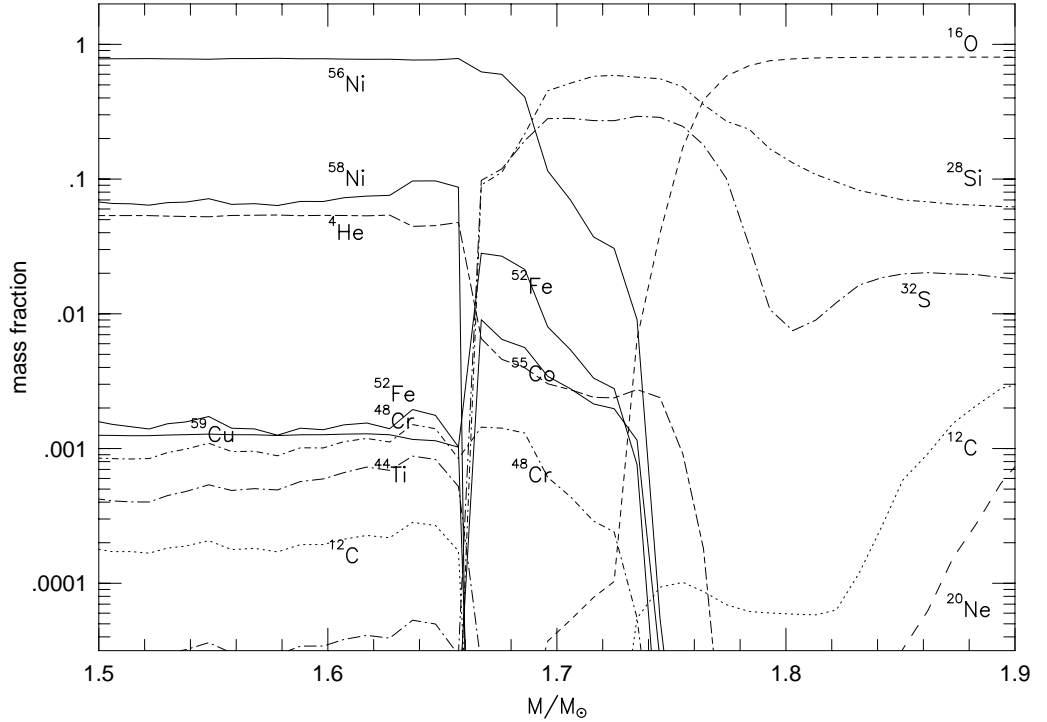


FIG. 3.— The isotopic composition of the ejecta from $20M_{\odot}$ stars ($6M_{\odot}$ He core).

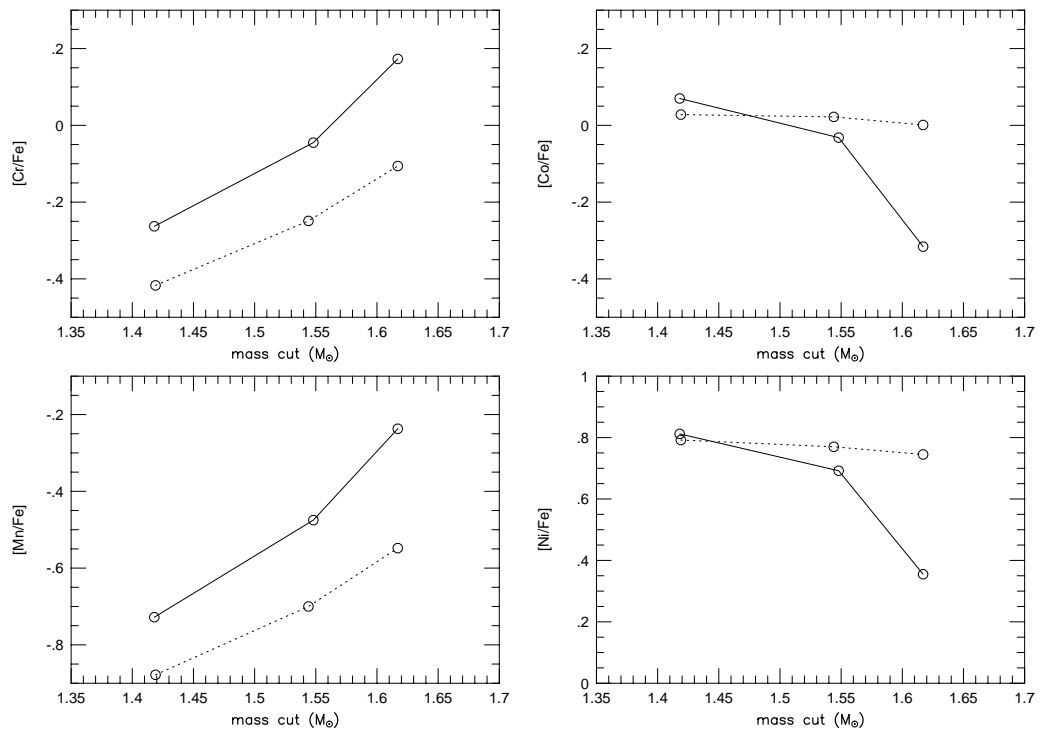


FIG. 4.— Dependence on mass cut. Three models with different mass cuts are used for each line. Solid line indicates supernovae of $M_{\text{core}} = 6M_{\odot}$, $E_{\text{exp}} = 1.0 \times 10^{51}$ ergs, $Y_e^{\text{deep}} = 0.4940$. Dotted line indicates that of $M_{\text{core}} = 8M_{\odot}$, $E_{\text{exp}} = 1.0 \times 10^{51}$ ergs, $Y_e^{\text{deep}} = 0.4985$.

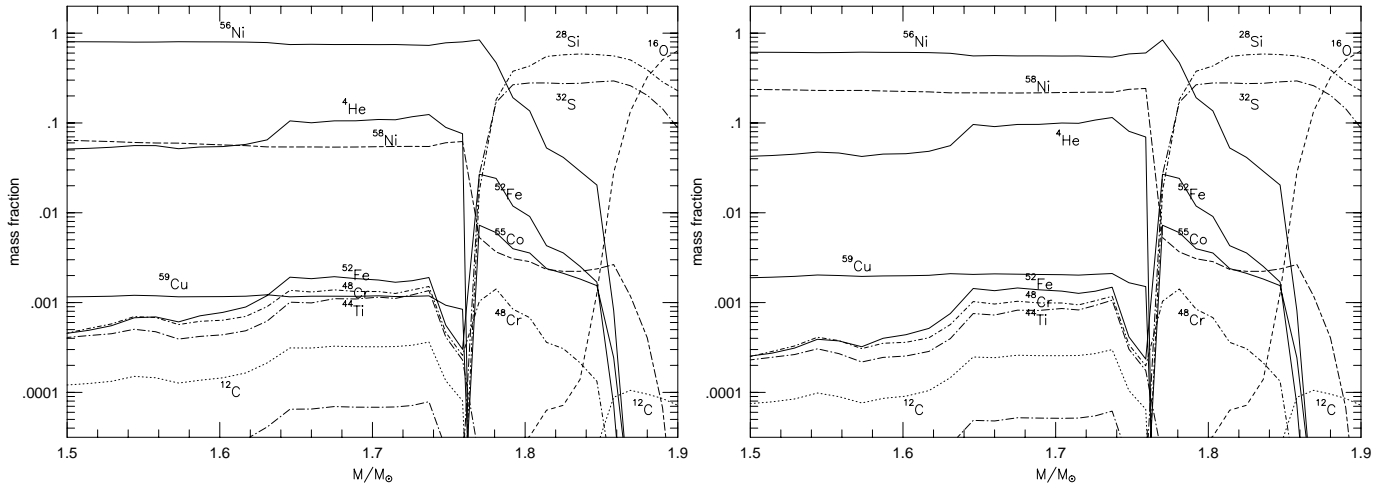


FIG. 5.— Dependence on Y_e . The progenitor is the $8M_\odot$ He core. The explosion energy is 1.0×10^{51} ergs. For both models, Y_e^{deep} is modified to be constant, 0.4985 (left) and 0.4950 (right).

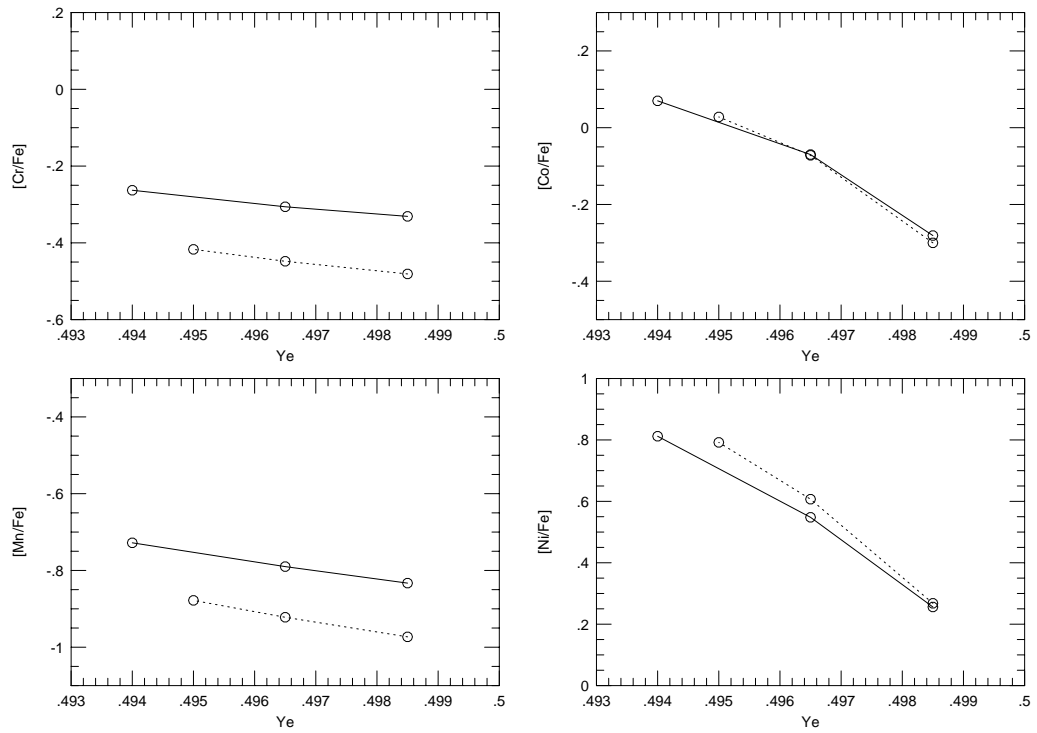


FIG. 6.— Dependence on Y_e . Three models with different Y_e are used for each line. Solid line indicates supernovae of $M_{\text{core}} = 6M_\odot$, $E_{\text{exp}} = 1.0 \times 10^{51}$ ergs, $M_{\text{cut}} = 1.418M_\odot$. Dotted line indicates $M_{\text{core}} = 8M_\odot$, $E_{\text{exp}} = 1.0 \times 10^{51}$ ergs, $M_{\text{cut}} = 1.419M_\odot$.

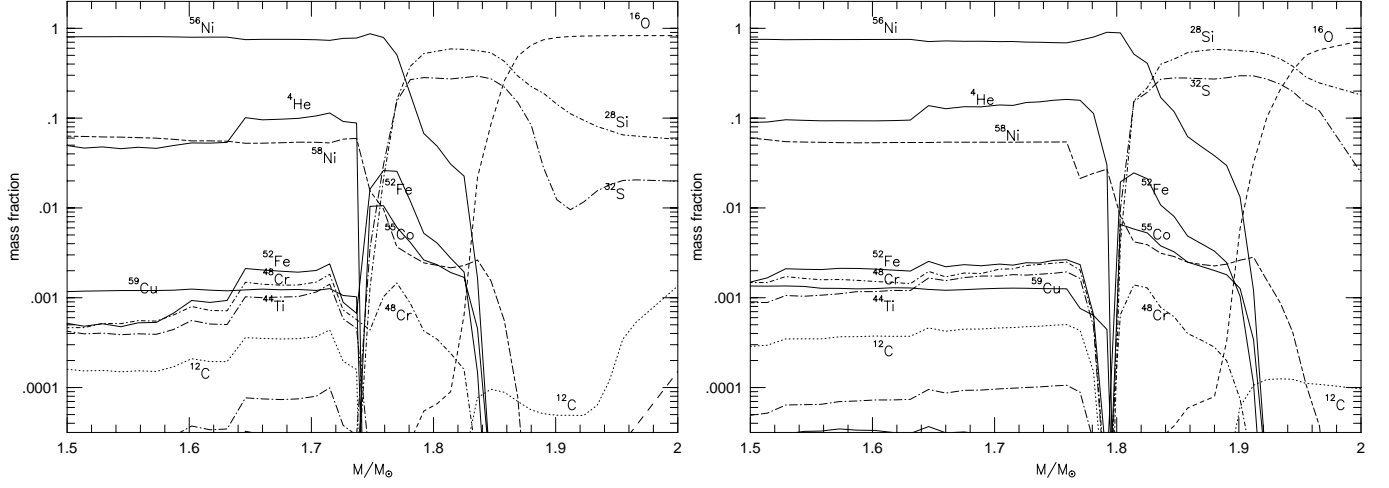


FIG. 7.— Dependence on explosion energy. They have the same progenitor the $8M_{\odot}$ He core and the Y_e^{deep} of 0.4985, but the explosion energies are 0.4×10^{51} ergs (left) and 2.0×10^{51} ergs (right).

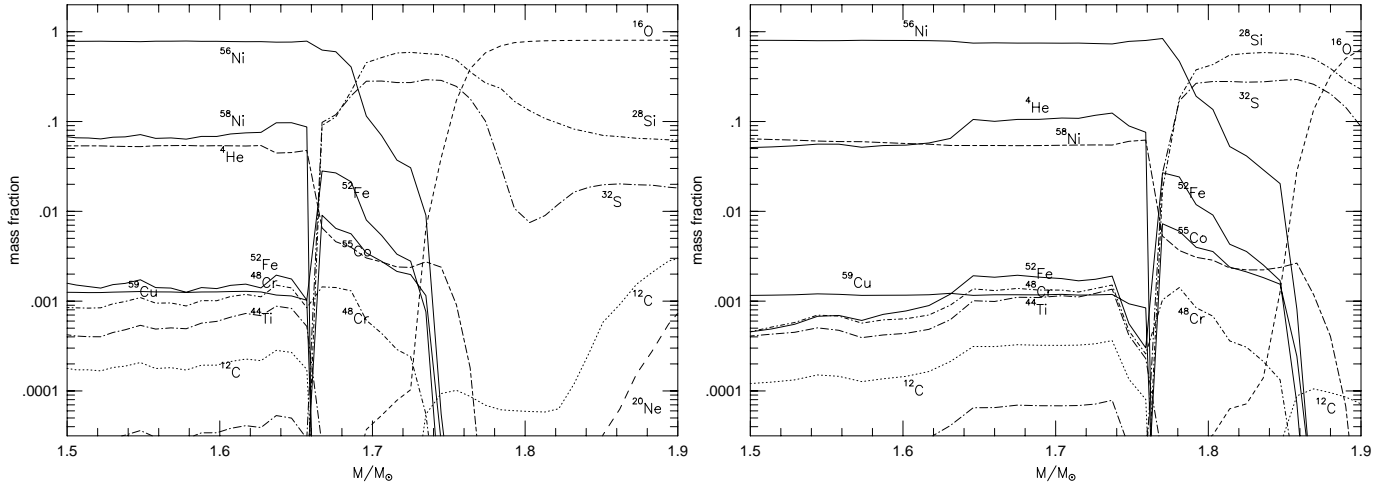


FIG. 8.— Dependence on progenitor mass. Both models have the same explosion energy of 1.0×10^{51} ergs and a Y_e^{deep} of 0.4985, but different progenitors, which are the $6M_{\odot}$ He core of the $20M_{\odot}$ star (left) and the $8M_{\odot}$ He core of the $25M_{\odot}$ star (right).

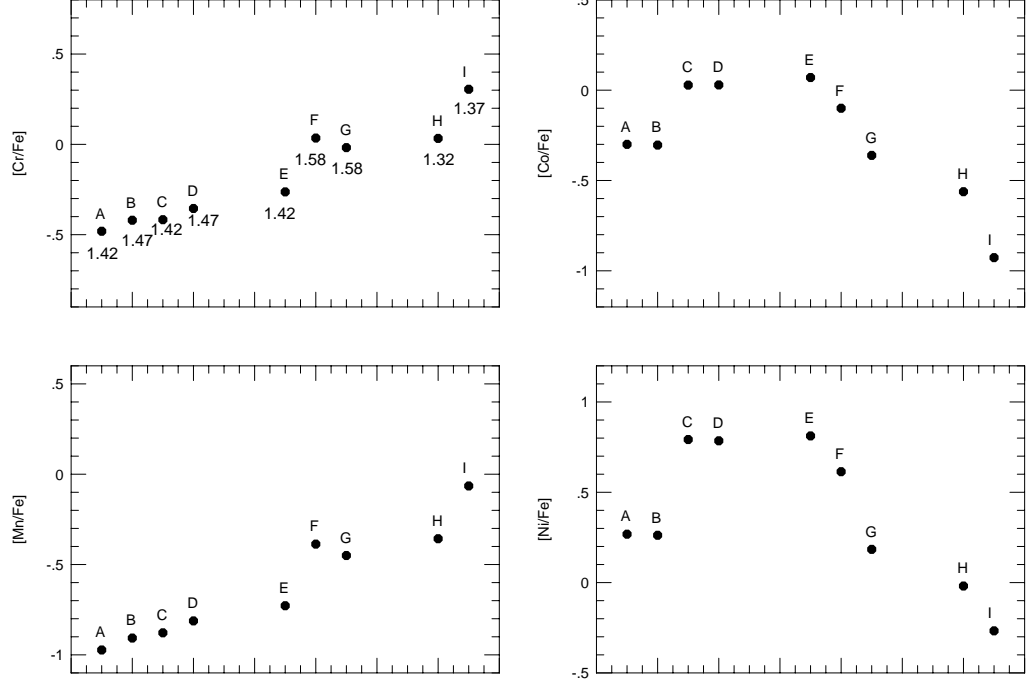


FIG. 9.— Abundance ratios of various SNe II. Mass cuts of the models are also shown below abundance ratios. Models **A** and **C** (**B** and **D**, **F** and **G**) have different Y_e^{deep} values (See Table 3).

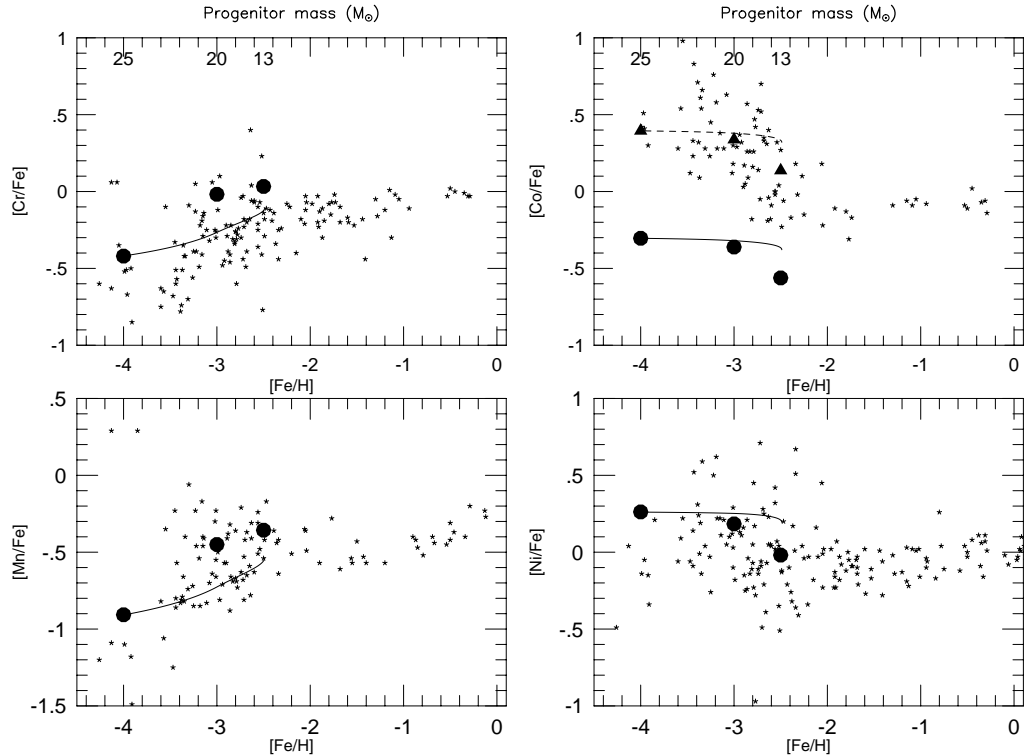


FIG. 10.— Variations in the iron-peak abundance ratios. The observational trend between ejected ^{56}Ni mass and stellar mass is taken into account. Solid lines and dashed line show ‘well-mixed’ models. ‘Unmixed models’ are also shown in filled circles and filled triangles. The models ‘B’, ‘G’ and ‘H’ in Figure 9 or Table 3 are used for obtaining these results. Dashed line and filled triangles indicate the models for which the Co yield is multiplied by five.

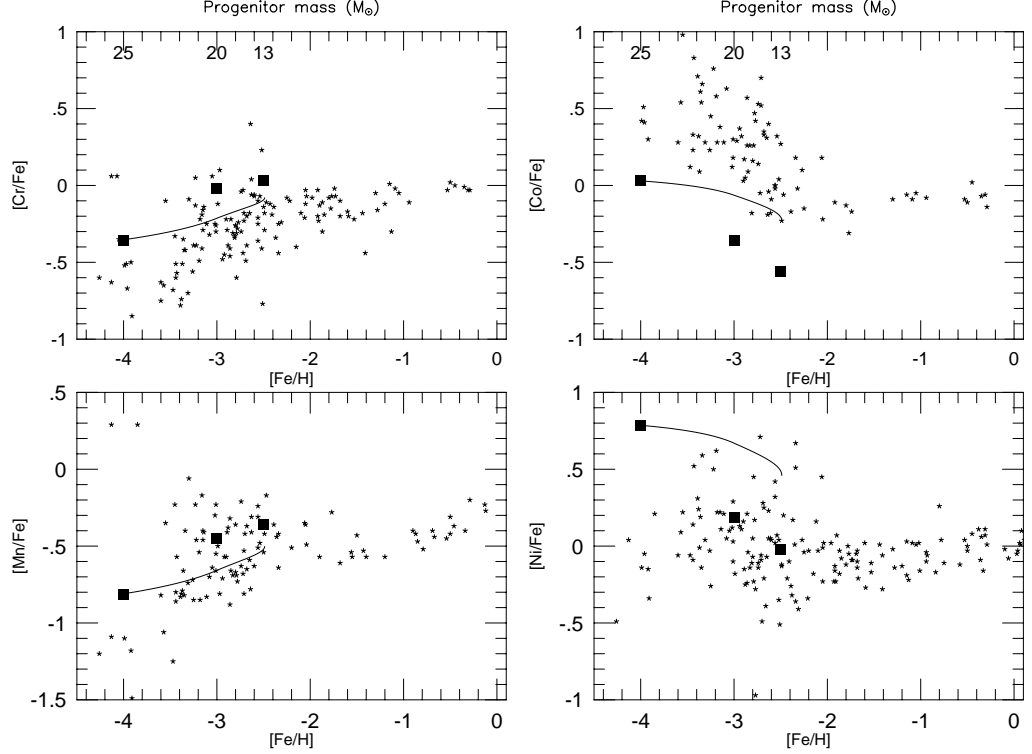


FIG. 11.— Variations in the iron-peak abundance ratios. Solid lines stand for ‘well-mixed’ models and filled squares for ‘unmixed models’. The models ‘D’, ‘G’ and ‘H’ in Figure 9 or Table 3 are used. The model ‘D’ has smaller Y_e^{deep} than ‘B’.

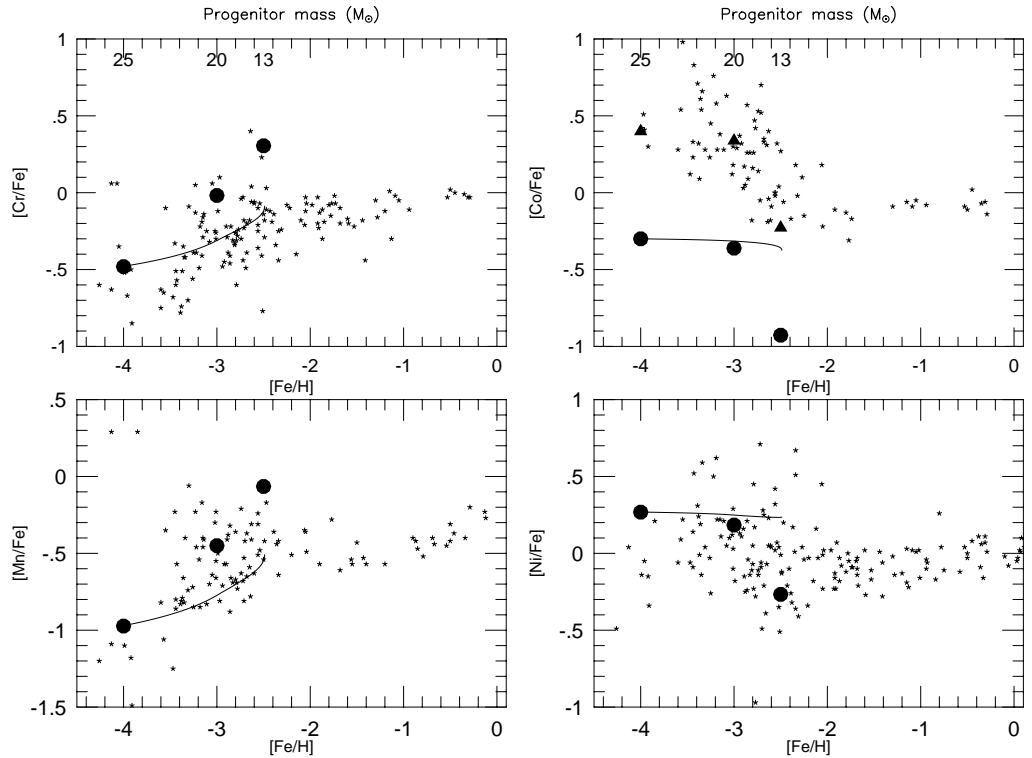


FIG. 12.— Same as Figure 10, but with models for making stronger contrast in abundance ratios. The models ‘A’, ‘G’ and ‘T’ in Figure 9 or Table 3 are used for solid lines and filled circles. Dashed line and filled triangles indicate the models for which the Co yield is multiplied by five.

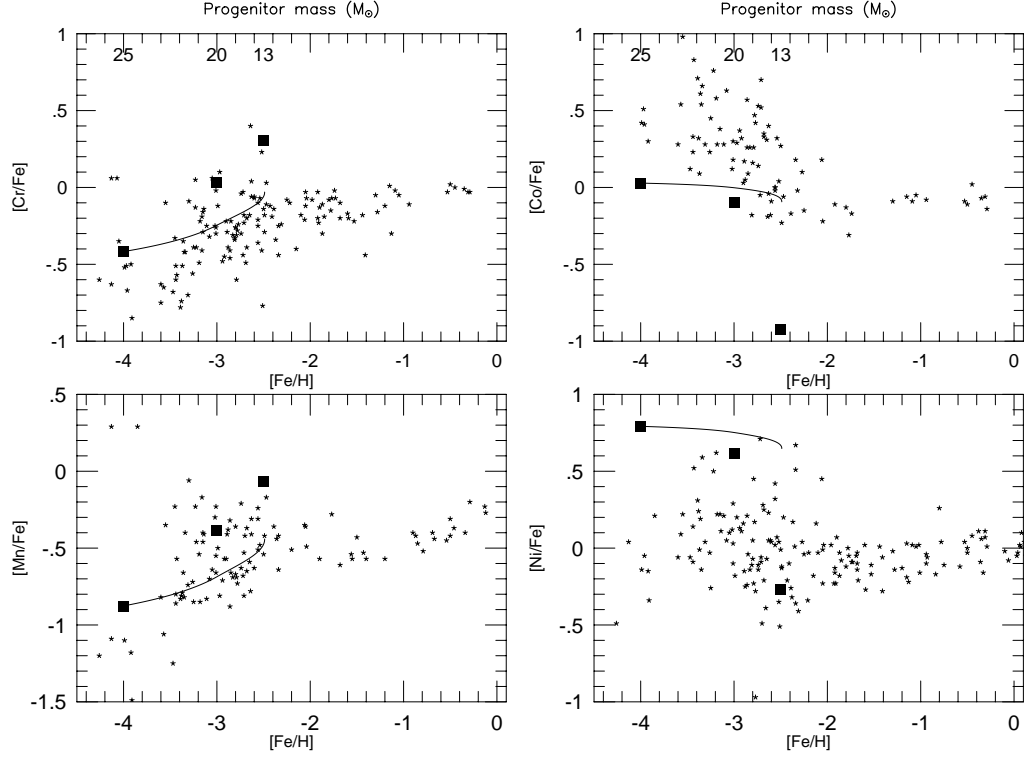


FIG. 13.— Same as Figure 11, but with models for making stronger contrast in abundance ratios. The models ‘C’, ‘F’ and ‘T’ in Figure 9 or Table 3 are used.

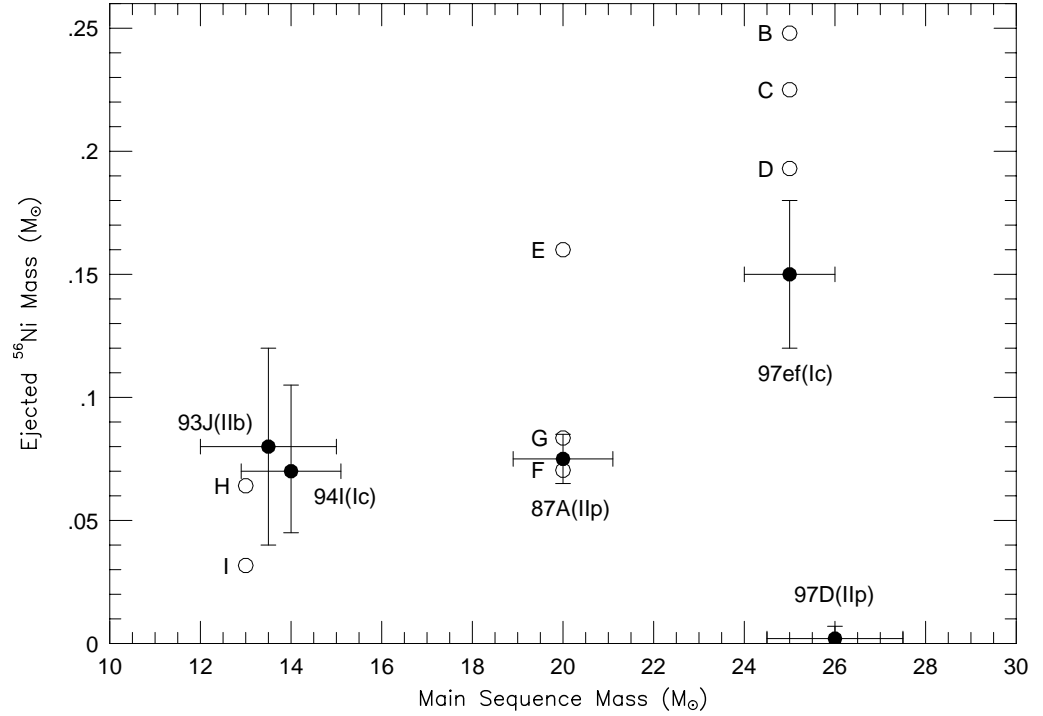


FIG. 14.— Ejected ^{56}Ni mass as a function of main sequence mass, e.g. Shigeyama et al. 1990 (SN1987A); Shigeyama et al. 1994 (SN1993J); Iwamoto et al. 1994 (SN1994I); Turatto et al. 1998 (SN1997D); Iwamoto et al. 1998 (SN1997ef). The ^{56}Ni mass of the models in Figure 9 are shown as open circles.

Model						
$M(M_\odot)$	25	25	25	20	20	20
$M_{\text{core}}(M_\odot)$	8	8	8	6	6	6
$E_{\text{exp}}(\times 10^{51} \text{ergs})$	1.0	1.0	1.0	1.0	1.0	1.0
$M_{\text{cut}}(M_\odot)$	1.42	1.54	1.62	1.42	1.55	1.62
Y_e^{deep}	0.4950	0.4950	0.4950	0.4940	0.4940	0.4940
Yield (M_\odot)						
Fe	2.44E-01	1.62E-01	1.14E-01	1.72E-01	9.53E-02	5.50E-02
Cr	1.30E-03	1.27E-03	1.24E-03	1.31E-03	1.20E-03	1.14E-03
Mn	3.38E-04	3.37E-04	3.37E-04	3.35E-04	3.34E-04	3.33E-04
Co	6.87E-04	4.84E-04	3.01E-04	5.33E-04	2.33E-04	7.00E-05
Ni	8.71E-02	5.48E-02	3.64E-02	6.42E-02	2.70E-02	7.16E-03
Ratio						
Cr/Fe	5.34E-03	7.87E-03	1.09E-02	7.62E-03	1.26E-02	2.08E-02
[Cr/Fe]	-0.417	-0.249	-0.106	-0.263	-0.044	0.173
Mn/Fe	1.38E-03	2.08E-03	2.96E-03	1.95E-03	3.50E-03	6.05E-03
[Mn/Fe]	-0.878	-0.700	-0.548	-0.728	-0.475	-0.273
Co/Fe	2.82E-03	2.77E-03	2.64E-03	3.10E-03	1.27E-03	2.45E-03
[Co/Fe]	0.028	0.022	0.001	0.070	-0.032	-0.316
Ni/Fe	3.57E-01	3.39E-01	3.20E-01	3.74E-01	2.83E-01	1.30E-01
[Ni/Fe]	0.792	0.770	0.745	0.812	0.692	0.355

TABLE 1

Dependence on mass cut.

Model						
$M(M_\odot)$	25	25	25	20	20	20
$M_{\text{core}}(M_\odot)$	8	8	8	6	6	6
$E_{\text{exp}}(\times 10^{51} \text{ergs})$	1.0	1.0	1.0	1.0	1.0	1.0
$M_{\text{cut}}(M_\odot)$	1.42	1.42	1.42	1.42	1.42	1.42
Y_e^{deep}	0.4950	0.4965	0.4985	0.4940	0.4965	0.4985
Yield (M_\odot)						
Fe	2.44E-01	2.71E-01	3.05E-01	1.72E-01	1.99E-01	2.21E-01
Cr	1.03E-03	1.35E-03	1.41E-03	1.31E-03	1.37E-03	1.44E-03
Mn	3.38E-04	3.38E-04	3.39E-04	3.35E-04	3.37E-04	3.38E-04
Co	6.87E-04	6.05E-04	4.03E-04	5.33E-04	4.47E-04	3.05E-04
Ni	8.71E-02	6.31E-02	3.26E-02	6.42E-02	4.05E-02	2.29E-02
Ratio						
Cr/Fe	5.34E-03	4.97E-03	4.61E-03	7.62E-03	6.89E-03	6.51E-03
[Cr/Fe]	-0.417	-0.448	-0.481	-0.263	-0.306	-0.331
Mn/Fe	1.38E-03	1.25E-03	1.11E-03	1.95E-03	1.69E-03	1.53E-03
[Mn/Fe]	-0.878	-0.922	-0.973	-0.728	-0.790	-0.833
Co/Fe	2.82E-03	2.34E-03	1.32E-03	3.10E-03	2.25E-03	1.38E-03
[Co/Fe]	0.028	-0.072	-0.300	0.070	-0.070	-0.281
Ni/Fe	3.57E-01	2.33E-01	1.07E-01	3.74E-01	2.03E-01	1.04E-01
[Ni/Fe]	0.792	0.607	0.268	0.812	0.548	0.256

TABLE 2

Dependences on Y_e .

Model	A	B	C	D	E	F	G	H	I
$M(M_\odot)$	25	25	25	25	20	20	20	13	13
$M_{\text{core}}(M_\odot)$	8	8	8	8	6	6	6	3.3	3.3
$E_{\text{exp}}(\times 10^{51} \text{ ergs})$	1.0	1.0	1.0	1.0	1.0	1.0	1.0	1.0	1.0
$M_{\text{cut}}(M_\odot)$	1.42	1.47	1.42	1.47	1.42	1.58	1.58	1.32	1.37
Y_e^{deep}	0.4985	0.4985	0.4950	0.4950	0.4940	0.4940	0.4985	0.4990	0.4990
Yield (M_\odot)									
Fe	3.05E-01	2.62E-01	2.44E-01	2.09E-01	1.72E-01	7.77E-02	9.01E-02	6.87E-02	3.50E-02
Cr	1.41E-03	1.39E-03	1.30E-03	1.29E-03	1.31E-03	1.18E-03	1.21E-03	1.04E-03	9.85E-04
Mn	3.40E-04	3.39E-04	3.38E-04	3.37E-04	3.35E-04	3.33E-04	3.34E-04	3.15E-04	3.14E-04
Co	4.03E-04	3.43E-04	6.85E-04	5.89E-04	5.33E-04	1.63E-04	1.03E-04	4.97E-05	1.09E-05
Ni	3.26E-02	2.75E-02	8.71E-02	7.36E-02	6.42E-02	1.84E-02	7.92E-03	3.79E-03	1.09E-03
^{56}Ni	2.90E-01	2.48E-01	2.25E-01	1.93E-01	1.60E-01	7.04E-02	8.35E-02	6.41E-02	3.17E-02
Ratio									
[Cr/Fe]	-0.481	-0.420	-0.418	-0.355	-0.263	0.035	-0.018	0.033	0.305
[Mn/Fe]	-0.973	-0.907	-0.878	-0.812	-0.728	-0.387	-0.450	-0.357	-0.065
[Co/Fe]	-0.300	-0.304	0.027	0.027	0.070	-0.100	-0.361	-0.562	-0.927
[Ni/Fe]	0.268	0.262	0.792	0.785	0.812	0.614	0.184	-0.019	-0.267

TABLE 3

SNe II in Figure 9.